Can Wang, An Deng, Abbas Taheri and Louis Ge

A mesh-free approach for multiscale modeling in continuum-granular systems

International Journal of Computational Methods, 2020; 17(10):2050006-1-2050006-27

A mesh-free approach for multiscale modeling in continuum–granular systems

Can Wang[1], An Deng[1*], Abbas Taheri[1], and Louis Ge[2]

[1] School of Civil, Environmental and Mining Engineering, University of Adelaide, Adelaide, SA 5005, Australia.

[2] Department of Civil Engineering, National Taiwan University, Taipei, Taiwan, 10617, China.

[*] Correspondence to: An Deng, School of Civil, Environmental and Mining Engineering, University of Adelaide, Adelaide, SA 5005, Australia. E-mail: an.deng@adelaide.edu.au

ABSTRACT

Geotechnical systems often examine interactions that occur between continuum bodies and granular soils. The systems and interactions can be accurately simulated by using multiscale coupling approaches. The model for the continuum bodies is often constructed into a mesh. The meshing however is time consuming for a huge spatial extent system and if distorted is subject to adjustments. A mesh-free approach can be used to eliminate these drawbacks. In this study, a mesh-free approach for simulating continuum–granular systems is presented. This approach combines element-free Galerkin (EFG) and discrete element (DE) methods to approximate the interactions. The capabilities of the coupled EFG–DE method are validated through its solving two example problems: the cantilever beam–disc system and Cundall's *Nine Disc Test*. The proposed approach appears to be an efficient and promising tool to model multiscale, multibody contacting problems.

Keywords: meshless, element-free Galerkin, discrete element, coupling, multiscale

1. INTRODUCTION

Multiscale modeling offers solutions, usually better than the solo scale (i.e., macro- or microscale) modeling, for geotechnical systems where a huge spatial continuum body presents in an assembly of granular soils [1, 2]. In these systems, multiscale modeling enables material response examinations at different scales of resolution, i.e. the macroscale approximation for the continuum bodies and microscale insight into the granular media [3]. To combine the multiscale examinations, coupling methods are applied. A usual coupling method is to develop the finite–discrete element models (FDEM) [4-9]. For the finite element analyses, meshing, re-meshing, or mesh distortion sometimes adds to the computational expenses or comprises the simulation accuracy [10-13]. Similar meshing problems occur to other mesh-based numerical methods, such as the finite difference [14, 15]. As suggested by Liu and Gu [16], meshless methods offer choices of solution for these meshing problems.

Meshless methods were developed in the 1970s with the intention of reducing engineers' dependence on meshes. Meshless methods emcompass a wide range of varieties, such as the natural element method [17], the scaled boundary method [18], and the element-free Galerkin (EFG) method [19]. Not until the 1990s, the EFG method was developed by Belytschko *et al.* [19] as a tool to predict fracture and crack growth. In this context, the crack propagation problem is modelled as an extending line. As the crack develops, the nodal points adjacent to the crack paths will lose their domain influence to the neighbouring nodes as they are separated. The EFG method defines a grid of nodes which are distributed over the problem domain (i.e, the continuum body), thus enabling a meshless representation of the body. Based on the nodes distribution, a shape function (for interpolations) is constructed. Where interpolations (for the inter-nodes) are needed, the EFG method uses the moving least square (MLS) approximation to establish algebraic expressions for the shape function. Overall the EFG method adopts an open, global form [16], that enables its uses in a range of engineering modeling problems [20-26].

The EFG method has been combined with other numerical tools in earlier studies. Most often, such as [27-29], the EFG method is combined with the finite element method in order to optimize domain meshing, improve computation efficiency and increase results accuracy. For example, Ullah *et al.* [30] used the finite element method to mesh the continuum domain at the outset and converted part of the domain into EFG nodes where necessary. In some other studies, such as [31-33], the EFG method can also be combined with the boundary method in order to improve the solution efficiency and to take the full advantages of the individual methods. These coupled approaches have proven successful in outperforming corresponding solo methods, however, are generally applicable to problems of continuum domain. The approaches are restricted, if not prohibited, from granular systems such as geomaterials, where the particulate nature is of interest and should be replicated.

In this study, the EFG method was coupled with the discrete element (DE) method to examine interactions that occur between continuum and graular bodies. The

EFG and DE modeling was applied to the two bodies respectively. The granular body comprised an assembly of discrete particles. The continuum–granular interfacial contacts were detected in terms of algorithms and used to transfer stresses and deformations between the bodies. The coupling method was validated through it solving two interesting example problems. To implement the method to the examples, the coupling was programmed and executed using the MATLAB software package. The single-platform programming avoids multiple-platform communications which multiscale modeling often use and prompts the computation efficiency.

2. GOVERNING EQUATIONS

In this section, the formulations that are established for the EFG and DE domains in a two-dimensional (2D) space are presented. The information obtained from the two domains is communicated at the domains interface, thus updating the resultant contact forces at each time step. The details of the algorithms developed for the transfer of forces are discussed. The responses at each of the nodes and particles in respective domains are examined.

2.1. Continuum domain

The continuum domain and its boundaries are represented by a grid of nodes. Although the method of nodes development and the choice of the domain shape are arbitrary, a grid of nodes in square, as shown in Figure 1, is usually used for simplification. The shape functions can be formed in a local support domain within the problem domain. The problem domain and the local support domain are represented by Ω and Ω_I respectively. Based on a Gauss quadrature rule [34], Gauss points are distributed in the background cell as illustrated so that the locations of the influenced nodes in the local domain are identified.

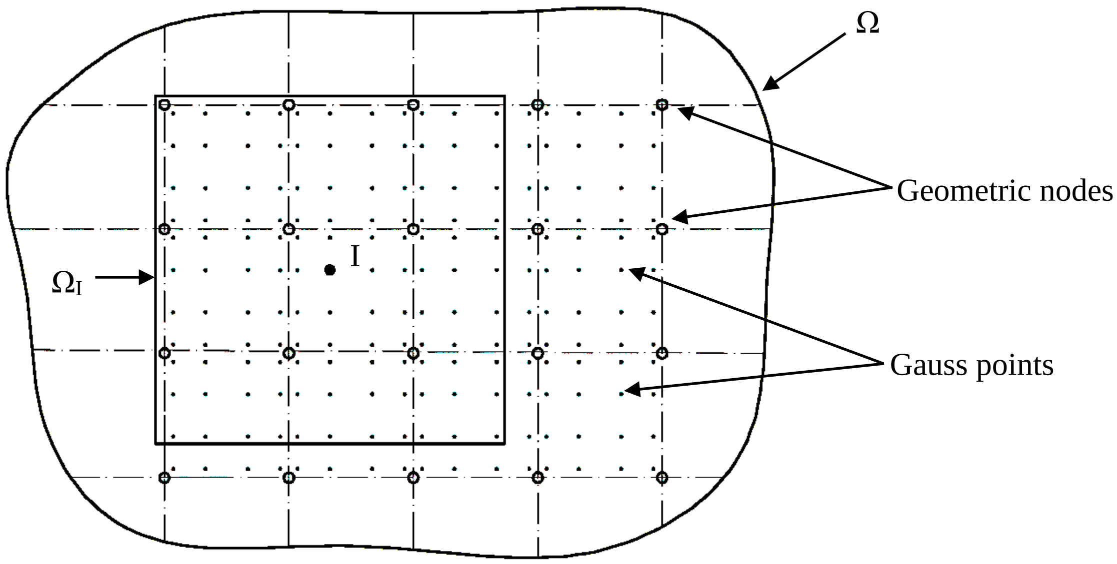

Figure 1. Schematic of the EFG domain presented by nodes and Gauss points.

The MLS approximation, as suggested in [16], is used to construct the shape functions. The MLS approximation applies to the local support domain Ω_I. As a set of equations are to be solved at the point of interest, an ill-conditioned system, where the solutions exist but difficult to find, may occur [22, 26]. To address this issue, an orthogonal basis function together with the MLS application is used to approximate the nodal displacement. Define the nodal displacement trial function, $u^h(x)$, as the approximation of the actual displacement, $u(x)$, at the point of interest. The trial function is written as:

$$u^h(x) = \sum_{j=1}^{m} q_j(x,\bar{x}) a_j(\bar{x}) \equiv \boldsymbol{q}^{\boldsymbol{T}}(\boldsymbol{x},\bar{\boldsymbol{x}})\boldsymbol{a}(\bar{\boldsymbol{x}}) \tag{1}$$

where $q_j(x,\bar{x})$ are the orthogonal basis functions corresponding to the monomial basis function $p(\boldsymbol{x})$, $a_j(\bar{x})$ are the coefficients, and m is the number of elements in the monomial basis function. To simplify the coupling framework with the DEM, a linear basis function in the 2D domain is created as:

$$\boldsymbol{p}^{\boldsymbol{T}}(\boldsymbol{x}) = [1, x, y] \tag{2}$$

By using the Schmidt method [35], the orthogonal basis function is obtained as:

$$q_k(x,\bar{x}) = p_k(x) - \sum_{j}^{k-1} \alpha_{kj}(\bar{x}) q_j(x,\bar{x}) \tag{3}$$

where, k=1 to 3, and the coefficient $a_{kj}(\bar{x})$ is expressed as:

$$\alpha_{kj}(\bar{x}) = \frac{\sum_{I}^{n} w_I(\bar{x}) p_k(x_I) q_j(x_I,\bar{x})}{\sum_{I}^{n} w_I(\bar{x}) q_j^{\,2}(x_I,\bar{x})} \tag{4}$$

where the index n refers to the nodes number in domain Ω_I, and $w_I(\bar{x})$ is the weight function and usually determined based on the exponential weight function or the conical weight function [19]. In this study, the cubic spine weight function [16] is adopted:

$$w(x - x_I) = w(r) = \begin{cases} 2/3 - 4r^2 + 4r^3 & r \le 0.5 \\ 4/3 - 4r + 4r^2 - (4/3)r^4 & 0.5 < r \le 1 \\ 0 & r > 1 \end{cases} \tag{5}$$

where $r = d_I / d_{mI}$, $d_I = |x - x_I|$, $d_{mI} = d_{max} \times c_I$, d_{max} is the scaling factor, and c_I can be defined as characteristic length of the integration zone that contains the point x_I. In a 2D space, the weight function is expressed as

$$w(x-x_I)=w(r_x)w(r_y)=w_x w_y \tag{6}$$

where r_x and r_y are calculated respectively as

$$r_x=\frac{|x-x_I|}{d_{mx}}=\frac{|x-x_I|}{d_{\max}c_{xI}} \tag{7}$$

$$r_y=\frac{|y-y_I|}{d_{my}}=\frac{|x-x_I|}{d_{\max}c_{xI}} \tag{8}$$

where d_{mx} and d_{my} are sizes of the support domain Ω_I, and c_{xI} and c_{yI} are coefficients calculated at node I by searching for nodes to satisfy the base function in both directions.

In the Hilbert space span q, for the selected point x and weight function w, the orthogonal function $q_j(x,\bar{x})$ should satisfy the expression as follows:

$$\sum_{I}^{m} w(x_I,\bar{x})q_k(x_I,\bar{x})q_j(x_I,\bar{x})=0 \tag{9}$$

where $m = 3$, $k \neq j$, and $k, j = I,\ldots, m$. In terms of the MLS approximation, the difference between the trial displacement $u^h(x)$ and actual displacement $u(x)$ should be minimized. Define the least square function as:

$$\begin{aligned} J &= \sum_{I=1}^{n} w(x-x_I)[u^h(x,x_I)-u(x_I)]^2 \\ &= \sum_{I=1}^{n} w(x-x_I)[q^T(x_I,\bar{x})a_i(\bar{x})-u(x_I)]^2, \end{aligned} \tag{10}$$

Minimizing J, the coefficients $a_j(\bar{x})$ are obtained as:

$$a_j(\bar{x})=\frac{\sum_{I=1}^{n} w_I(\bar{x})q_j(x_I,\bar{x})u_I}{\sum_{I=1}^{n} w_I(\bar{x})q_j^2(x_j,\bar{x})}, \quad j=1 \text{ to } m \tag{11}$$

Applying the MLS approximation, we have:

$$u^h(x)=\sum_{I}^{n}\phi_I(x)u_I \tag{12}$$

Therefore the shape function $\phi_I(x)$ is defined as:

$$\phi_I(x) = w_I(x)\sum_{j}^{m} \frac{q_j(x,x)q_j(x_I,x)}{\sum_{I}^{n} w_I(\bar{x})q_j^{\,2}(x_I,\bar{x})} \tag{13}$$

The partial derivative of the shape function is expressed as:

$$\phi_{I,k}(x) = w_{I,k}(x)\sum_{j}^{m} \frac{q_j(x,x)q_j(x_I,x)}{\sum_{I}^{n} w_I(\bar{x})q_j^{\,2}(x_I,\bar{x})} + w_I(x)\sum_{j}^{m} \frac{A1 - A2}{[\sum_{I}^{n} w_I(\bar{x})q_j^{\,2}(x_I,\bar{x})]^2} \tag{14}$$

where the subscript '*k*' denotes partial derivative to *x* or *y*, and parameters *A*1 and *A*2 are expressed respectively as

$$A1 = \sum_{I}^{n} w_I(x)q_j^{\,2}(x_I,x)[q_{j,k}(x,x)q_j(x_I,x) + q_j(x,x)q_j(x_I,x)] \tag{15}$$

$$A2 = q_j(x,x)q_j(x_I,x)[\sum_{I}^{n} w_{I,k}(x)q_j^{\,2}(x_I,x) + 2\sum_{I}^{n} w_I(x)q_j(x_I,x)q_{j,k}(x_I,x)] \tag{16}$$

Note that $w_I(x)$, $q_j(x,x)$ and $q_j(x_I,x)$ are derivable with respect to *x*.

2.2. Dynamic equation

According to Liu and Gu [16], the dynamic equation for node *I* in the local domain is expressed as:

$$\int_{\Omega_I} \widehat{W}_I(\sigma_{ij,j} + b_i - \rho\ddot{u}_i - c\dot{u}_i)d\Omega = 0 \tag{17}$$

where $\widehat{W}_I$ is the weight function. In a discretized system, the dynamic equation for node *I* is written as:

$$\mathbf{M_I\ddot{u}(t) + C_I\dot{u}(t) + K_Iu(t) = F_I(t)} \tag{18}$$

where $\mathbf{M_I}$, $\mathbf{K_I}$ are the local mass and stiffness matrix respectively for node *I*, $\mathbf{C_I}$ is the corresponding damping matrix, $\mathbf{F_I}$ is the force acting on node *I* at time t, and $\mathbf{u_I(t)}$, $\mathbf{\dot{u}_I(t)}$, $\mathbf{\ddot{u}_I(t)}$ are nodal displacement, velocity and acceleration at time *t*.

On the traction boundary Γ_t, the boundary conditions are written as:

$$\sigma \cdot \mathbf{n} = \bar{\mathbf{t}} \tag{19}$$

where σ is the stress tensor**,** $\mathbf{n}$ is the unit normal to the domain Ω, and $\bar{\mathbf{t}}$ are the prescribed tractions. On the displacement boundary $\Gamma_{\mathbf{u}}$, the boundary conditions become

$$\mathbf{u} = \bar{\mathbf{u}} \tag{20}$$

where $\bar{\mathbf{u}}$ are the prescribed displacements. In order to satisfy the boundary conditions, as suggested in Liu and Gu [16], the penalty method (i.e., optimization algorithms) is adopted for simplicity and also maintain the symetrical matrix. By introducing the penalty coefficient α [26], the Galerkin form [16] for a dynamic problem is written as:

$$\int_{\Omega} \delta\, \mathrm{u}^{\mathrm{T}} \rho\, \ddot{\mathbf{u}}\, \mathrm{d}\Omega + \int_{\Omega} \delta\, \mathrm{u}^{\mathrm{T}} c\, \dot{\mathbf{u}}\, \mathrm{d}\Omega + \int_{\Omega} \delta\, \varepsilon^{\mathrm{T}} \sigma \mathrm{d}\Omega - \int_{\Omega} \delta\, \mathrm{u}^{\mathrm{T}} \mathrm{b} \mathrm{d}\Omega - \int_{\Gamma_{\mathbf{t}}} \delta\, \mathrm{u}^{\mathrm{T}}\, \bar{\mathbf{t}}\, \mathrm{d}\Gamma + \int_{\Gamma_{\mathbf{u}}} \delta\, \mathrm{u}^{\mathrm{T}} \alpha (\mathrm{u} - \bar{\mathbf{u}}) \Gamma = 0 \tag{21}$$

where δ is the test function, and $\boldsymbol{\alpha} = \begin{bmatrix} \alpha_1 & 0 \\ 0 & \alpha_2 \end{bmatrix}$. The penalty factors α_i are usually assigned a constant, large, positive number, and this study adopts $\alpha_i = 10^5 \times \mathrm{E}$. Using Eq. (21), the discretized function for a dynamic problem can be developed. The detailed process was discussed in Zhang *et al.* [26], and is expressed as:

$$\mathbf{M}\ddot{\mathbf{U}} + \mathbf{C}\dot{\mathbf{U}} + (\mathbf{K} + \mathbf{K}^{\boldsymbol{\alpha}})\mathbf{U} = \mathbf{F} + \mathbf{F}^{\boldsymbol{\alpha}} \tag{22}$$

In Eq. (22), $\mathbf{U}$, $\dot{\mathbf{U}}$ and $\ddot{\mathbf{U}}$ are global vectors for displacement, velocity and acceleration of all of the nodes, respectively; **M** and **K** are respectively the mass matrix and stiffness matrix in the problem domain, **C** is the damping matrix, **F** is the global external force vector, $\mathbf{K}^{\boldsymbol{\alpha}}$ is the global penalty matrix, and the additional force vector $\mathbf{F}^{\boldsymbol{\alpha}}$

is derived from the boundary conditions. And, these parameters are expanded as:

$$\mathbf{M_{IJ}} = \int_{\Omega} \mathbf{\Phi_I^T} \rho \mathbf{\Phi_J} \mathrm{d}\Omega \tag{23}$$

$$\mathbf{C_{IJ}} = \int_{\Omega} \mathbf{\Phi_I^T} c \mathbf{\Phi_J} \mathrm{d}\Omega \tag{24}$$

$$\mathbf{K_{IJ}} = \int_{\Omega} \mathbf{B_I^T D B_J d}\Omega \tag{25}$$

$$\mathbf{K_{IJ}^{\alpha}} = \int_{\mathbf{\Omega}} \mathbf{B_I^T} \boldsymbol{\alpha} \mathbf{B_J} \mathrm{d}\Omega \tag{26}$$

$$\mathbf{F} = \int_{\mathbf{\Omega}} \mathbf{\Phi_I^T b} \mathrm{d}\Omega + \int_{\mathbf{\Gamma_t}} \mathbf{\Phi_I^T} \bar{\mathbf{t}} \mathrm{d}\Gamma \tag{27}$$

$$\mathbf{F}^{\boldsymbol{\alpha}} = \int_{\mathbf{\Gamma_u}} \mathbf{\Phi_I^T} \boldsymbol{\alpha} \bar{\mathbf{u}} \mathrm{d}\Gamma \tag{28}$$

where c is the damping coefficient, and the other coefficients are defined as follow:

$$\mathbf{\Phi_I} = \begin{bmatrix} \phi_I & 0 \\ 0 & \phi_I \end{bmatrix} \tag{29}$$

$$\mathbf{B} = \begin{bmatrix} \phi_{I,1} & 0 \\ 0 & \phi_{I,2} \\ \phi_{I,1} & \phi_{I,2} \end{bmatrix} \tag{30}$$

and, for plan stress problems,

$$\mathbf{D} = \frac{E}{1-v^2} \begin{bmatrix} 1 & v & 0 \\ v & 1 & 0 \\ 0 & 0 & (1-v)/2 \end{bmatrix} \tag{31}$$

for plan strain problems,

$$\mathbf{D} = \frac{E}{(1+v)(1-2v)} \begin{bmatrix} 1-v & v & 0 \\ v & 1-v & 0 \\ 0 & 0 & (1-2v)/2 \end{bmatrix} \tag{32}$$

2.3. Granular domain

In the granular domain, the interaction between the particles, or the particles and wall, is determined based on Newton's second law of motion and the force–displacement law. The two laws govern the motion of the entities of interest and update the contact force based on the displacement. Similar to the dynamic problem described in Eq. (18), in the granular domain, as per Cundall and Strack [36], the particle motion is expressed as:

$$m_{p,i}\ddot{\mathbf{u}}_{\mathbf{i}}(\mathbf{t}) + c\,\dot{\mathbf{u}}_{\mathbf{i}}(\mathbf{t}) = \mathbf{F}_{\mathbf{i}}(\mathbf{t}) \tag{33}$$

$$I_i\ddot{\boldsymbol{\theta}}_{\mathbf{i}}(\mathbf{t}) + c^*\dot{\boldsymbol{\theta}}_{\mathbf{i}}(\mathbf{t}) = \mathbf{M}_{\mathbf{i}}(\mathbf{t}) \tag{34}$$

where $m_{p,i}$ is the mass of disc i, I_i is the moment of inertia of disc i, $\dot{\mathbf{u}}_{\mathbf{i}}(\mathbf{t})$ and $\dot{\boldsymbol{\theta}}_{\mathbf{i}}(\mathbf{t})$ are respectively the translational and angular velocities for disc i, c and c^* are global damping coefficients for translational and rotational velocities, respectively, and $\mathbf{F}_{\mathbf{i}}(\mathbf{t})$ and $\mathbf{M}_{\mathbf{i}}(\mathbf{t})$ are resultant force and moment at contact, respectively.

The DE model uses a set of mechanical elements (e.g., a spring and dashpot) to calculate the contact force occurred between two entities (or particles) of interest. One of the widely used models is the linear contact, as presented in Figure 2. A finite overlap is allowed between the rigid particles to simulate the particle's deformation. The dashpot element is used to reflect viscous behavior at contact. The contact force is determined in terms of the deformation of these mechanical elements, or the relative displacement between the particles. In the model, the normal and shear forces between the entities i and j, F_{ij}^n and F_{ij}^s, respectively, are calculated as:

$$F_{ij}^n = k_n\Delta n + \beta k_n \Delta n \tag{35}$$

$$F_{ij}^s = k_s\Delta s + \beta k_s \Delta s \tag{36}$$

where k_n and k_s are contact normal and shear stiffness respectively, Δn and Δs are relative displacements measured at the normal and shear directions, and β is a damping coefficient. To model the stick–slip contact occurred between entities, a Coulomb–friction criterion is employed as follows:

$$(F_{ij}^{s})_{\max} \leq F_{ij}^{n} \tan \varphi_u + c \tag{37}$$

where $(F_{ij}^{s})_{\max}$ is the maximum value of the shear force, φ_u is the smaller of the interparticle friction angles for entities i and j, and c is the smaller of entities' cohesion. The moment acting on entity i is the result of all the shear forces applied at its contacts and is expressed as:

$$M_i = \sum_{j=1}^{n} F_{ij}^{s} r_i \tag{38}$$

where r_i is the radius of entity i.

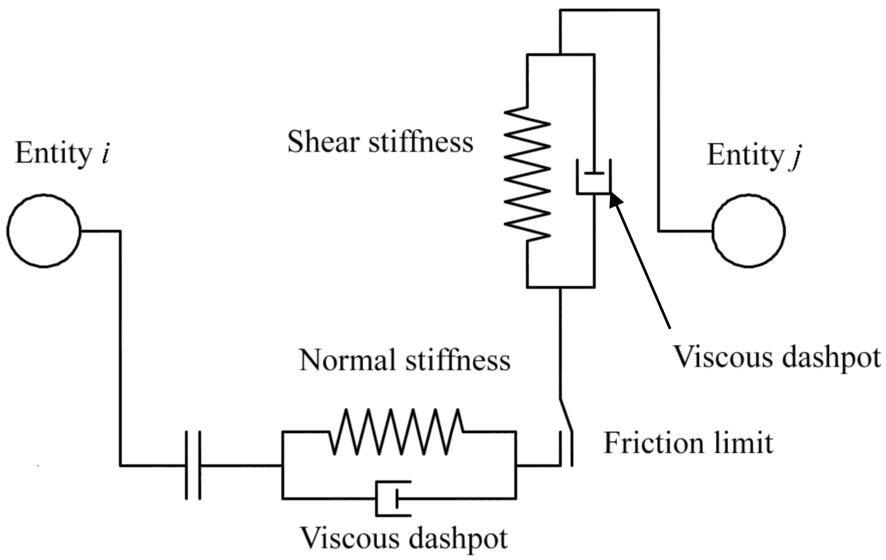

Figure 2. Schematic of the linear contact model used in DEM.

2.4. Continuum–granular interface

The continuum–granular domain interface is examined to communicate the force–displacement relationship between the two domains. The domains interface is modeled as the disc–wall (or segment) contact, which is commonly used in the FDEM analyses (e.g. Nakashima and Oida [37]). Specifically, the interface becomes disc–segment contacts. At each contact, paired disc–segment contact forces are transmitted to the disc centroid and the nodes of each element at the interface. A bonding strength can be specified to transmit a tensile strength or a moment. The forces travel to the rest parts of corresponding domains.

A similar concept is used in the EFG–DE domain interface as follows: *a*) detect the valid contacts between discs (of granular domain) and segments (of continuum domain), including contact forces and their positions; and *b*) compute the external force matrix arising from the contacts. The computer flow chart is represented in Figure 3. It is noted that the EFG–DE method processes the interface force in a way different from that for the FDEM method. The granular contact force cannot be transmitted directly to the node forces at the interface, as the shape function obtained does not have Kronecker delta function property [16]. A new approach is developed to transmit the forces.

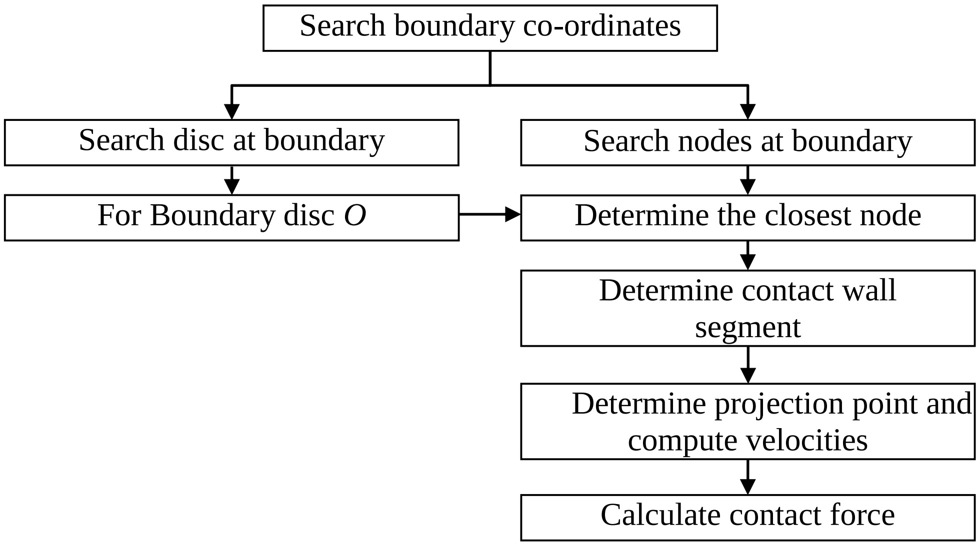

Figure 3. The computer flow chart used to determine the interface force.

2.4.1. Contact detection

Contacts occur in two forms: the disc–disc contacts in the granular domain and the disc–segment on the domains interface. The former type of contact can be detected in commercially accessible software packages, e.g. the *PFC*, or an open source code such as *Escript* [38] or *Yade*. These packages however are not established to readily detect the disc–segment contacts, or otherwise have to use a bridging scheme [39] to communicate contact detections across the domains. There are algorithms [11, 12, 40] developed to detect finite–discrete element interfacial contacts. These algorithms, however, are not applicable to the EFG–DE interface and a separate approach is required. To these ends, we developed contact detection algorithms in terms of Muth *et al.* [41] and programmed the algorithms on the *MATLAB* platform.

To detect the EFG–DE interfacial contacts, the first step is to gather location information for the nodes and discs adjacent to the interface. Figure 4 illustrates disc *O* and nodes *i* to *i*+*N* which contact and sit on the interface. To detect the disc–segment contact, the following subroutines are executed: *a*) Calculate $d_{i,O}$, the distance between centroid *O* and node *i* , where *i*=*i*,…,*i*+*N*; *b*) Determine the minimum distance $(d_{i,O})_{min}$ and the corresponding node number *j*; *c*) Calculate distances $d_{j-1,O}$ and $d_{j+1,O}$; *d*) Determine the interface segment. The segment is section (*j*–1, *j*) if $d_{j-1,O} > d_{j+1,O}$, or section (*j*, *j*+1) if $d_{j-1,O} < d_{j+1,O}$. If $d_{j-1,O} = d_{j+1,O}$, the segment is dependent on the distance between the centroid and the segments of interest which is discussed in the next paragraph; *e*) Calculate $d_{H,O}$, the distance between centroid *O* and point *H*. Line *OH* is drawn normal to the segment determined in Step *d*); and *f*) Calculate the velocity at point *H* based on the shape function of this segment, and the velocity of nodes *j* and *j*–1 based on the EFG method.

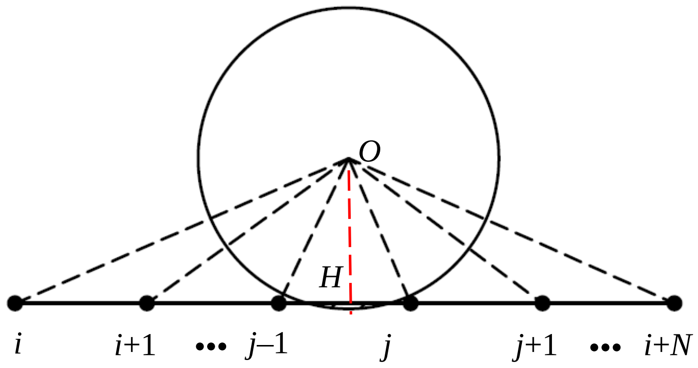

Figure 4. An illustration of disc position and boundary line segments.

The next step is to determine the contact geometric primitives. In the FDEM coupling work, Zang *et al.* [11] categorized the contact geometric primitives into particle–facet, particle–edge and particle–vertices problems. These contacts are not suitable to the EFG–DE coupling. Instead, two types of disc–segment contacts are discussed, as shown in Figure 5(a) and (b) respectively. Figure 5(a) shows the particle–segment contact where no nodes sit within the interface segment. Figure 5(b) shows the particle–point contact where disc O contacts node j. At the particle–point contact, the segment (j–1, j+1) deforms into two sub-segments, (j–1, j) and (j, j+1). In this case, the contact force will be doubled. To eliminate this error, distance $d_{H,O}$ is replaced by $d_{j,O}$ in Step *f*) in the contact detection subroutine.

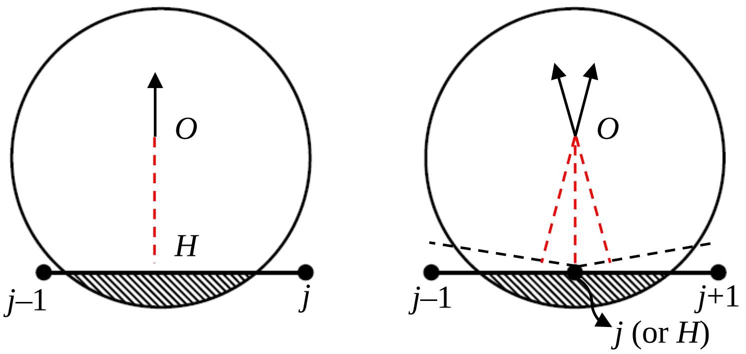

(a) (b)

Figure 5. Schematic of disc–segment contact: (a) particle–segment contact, and (b) particle–point contact.

Based on the finite difference method, the discrete equation used to calculate the increment of disc–segment force is written as:

$$\Delta F_{HO}^{n} = k_n (v_O - v_H)\Delta t + \beta k_n (v_O - v_H)\Delta t \tag{39}$$

$$\Delta F_{HO}^{s} = k_s (v_O - v_H)\Delta t + \beta k_s (v_O - v_H)\Delta t \tag{40}$$

where v_o and v_H are the average velocities of centroid O and point H on the segment during time step Δt. The velocity of v_H is expressed as:

$$v_H = v_i + \frac{l_{i,H}}{l_{i,i+1}}(v_{i+1} - v_i) \tag{41}$$

or, if $d_{j-1,O} = d_{j+1,O}$, is simplified into

$$v_H = v_i \tag{42}$$

where v_i and v_{i+1} are the velocity of nodes i and i+1 respectively, $l_{i,H}$ is the distance between nodes i and H, and $l_{i,i+1}$ is the distance between nodes i and i+1.

2.4.2. Determination of contact force

In finite element modeling, contact forces are usually acted as a point load on the boundary nodes [42]. This point-load approach cannot be directly applied to the boundary nodes in the EFG domain, which otherwise invalidates the use of MLS approximation [19]. Alternatively, each load is regarded as a distributed traction, and multiple tractions are superposed. According to Zuohui [43], if a point load F acts at position (x_0, y_0) on interface Γ_t as shown in Figure 6, the following equation is obtained:

$$\int_{\Gamma_t} \mathbf{\Phi}_I^T t_i \mathbf{d}\Gamma = \int_{\Gamma_t} \mathbf{\Phi}_I^T F_i \delta(x - x_i) \mathbf{d}\Gamma = \mathbf{\Phi}_i^T F_i \tag{43}$$

where δ is the Dirac delta function. Assuming a total of N point loads act on the boundary, the superposed traction is expressed as:

$$\bar{t}(x) = \sum_{i=1}^{N} t_i = \sum_{i=1}^{N} F_i \delta(x - x_i) \tag{44}$$

Eq. (43) then becomes as

$$\int_{\Gamma_t} \mathbf{\Phi}_I^T \bar{t} d\Gamma = \sum_{i=1}^{N} \mathbf{\Phi}_i^T F_i \tag{45}$$

Substituting Eq. (45) to Eq. (27) leads to:

$$\mathbf{F}=\int_{\Omega}\mathbf{\Phi}_{\mathbf{I}}^{\mathbf{T}}\mathbf{b}\mathrm{d}\mathbf{\Omega}+\sum_{i=1}^{N}\int_{\Gamma_t}\mathbf{\Phi}_{\mathbf{I}}^{\mathbf{T}}F_i\delta(x-x_i)\mathrm{d}\mathbf{\Gamma}=\int_{\Omega}\mathbf{\Phi}_{\mathbf{I}}^{\mathbf{T}}\mathbf{b}\mathrm{d}\mathbf{\Omega}+\sum_{i=1}^{N}\mathbf{\Phi}_{\mathbf{I}}^{\mathbf{T}}F_i \tag{46}$$

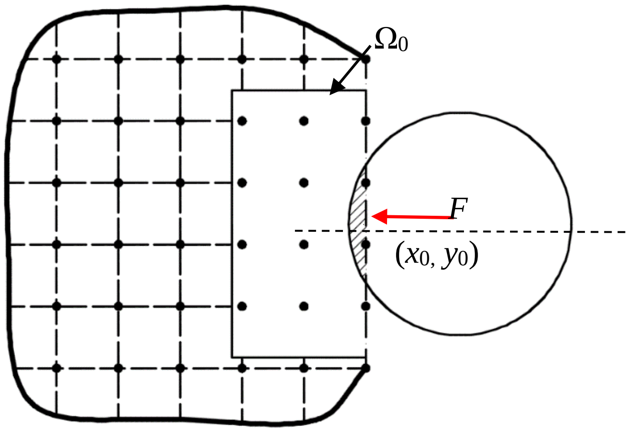

Figure 6. The interaction between a disc and an EFG domain.

In Eq. (46), the external force F acting on domain Ω contains two components: the body force such as the gravity, and the point load. The latter part of the equation refers to the following physical meaning: when a point load F_i acts at point (x_0, y_0) on a continuum boundary, this load is distributed to the surrounding points in the local supporting domain Ω_I based on shape function $\phi_I(x)$ which is determined by Eq. (13). The supporting domain area may be affected by the chosen domain scaling factor d_{max}.

3. TIME INTEGRATION

In the EFG–DE simulation, the force–displacement relationship is discretized into finite time steps. To enable a converge of the simulation, the value of the time steps is properly determined to ensure the algorithms are stable in both DE and EFG domains. This section describes the method developed to determine the time step and to present the corresponding governing equations in the two domains.

3.1. Time step

A time step is determined either explicitly or implicitly. Belytschko *et al.* [44] discussed the differences between the explicit and implicit methods and suggested that the choice of method should be determined in terms of the governing equations, smoothness of data, and material response to examine. In the discrete element analysis, the central difference method is often used [36]. This method guarantees numerical stability so that each time step does not exceed the critical time step in the explicit time scheme. Also when the particle number increases, the implicit time schemes may require solving multiple matrices at each time step, which significantly increases the processing time [45]. Due to the above reasons, one common method in the coupled model is to determine the time step using explicit–explicit schemes [12, 40], which is expressed as:

$$\Delta t \le \min\left(\Delta t_1, \Delta t_2\right) \tag{47}$$

where Δt_1 and Δt_2 are the minimum time steps in the continuum and granular domains, respectively. To optimize the time step determination, Elmekati and El Shamy [46] suggested to use the predictor–corrector method, a two-staged iterative process. This method arises from the fact that Δt_2 is usually much less than Δt_1. Therefore the time step in the main routine is expressed as Δt_1:

$$\Delta t = \Delta t_2 = n\Delta t_1 = n\sqrt{\frac{m_p}{K}} \tag{48}$$

where n is an integer, m_p is the particle mass, and K is the contact spring stiffness.

In this present study, an explicit–implicit time integration scheme was adopted. In the continuum domain, the iterations are stable due to the advantages of the implicit method, if relatively a small- to medium time step increment is used [26]. Therefore, time steps only need to be determined in the DE domain. Also, the calculation is consistent in the combined model because the results of the DE simulation can be transmitted to the EFG domain at each time step. In this context, important information such as the contact detection on the interface should be attained, so that the conditions at each node and particle can be examined explicitly while executing major iterations.

3.2. Partial difference solution

Difference method is used to discretize the time domain to solve governing equations. The governing equations relating to accelerations, velocities and displacements arising from the force acting on the two domains are updated at each time step. It is noteworthy that the governing equations for the two domains are solved in different processes. The differences are illustrated in Figure 7. In the EFG domain, the governing equations are solved based on a matrix, which arises from the nature of continuum body. In the DE domain, stiffness matrix dimensions may vary in different steps as some particles may not in contact as shown in Figure 7 (b). Therefore, the contact conditions need to be determined at the end of each step. It is computationally expensive to compute a stiffness matrix at each loop. Where appropriate the responses of individual particles are examined, which avoids excessive iterations of the stiffness matrix. In the EFG domain, the nodes are numbered sequentially and the displacement, velocity and acceleration are obtained in matrices (i.e. $\mathbf{U}$, $\dot{\mathbf{U}}$ and $\ddot{\mathbf{U}}$ respectively). In the DE domain, the displacement, velocity and acceleration are calculated for disc *i*, i.e., u_i, $\dot{u}_i$ and $\ddot{u}_i$ respectively.

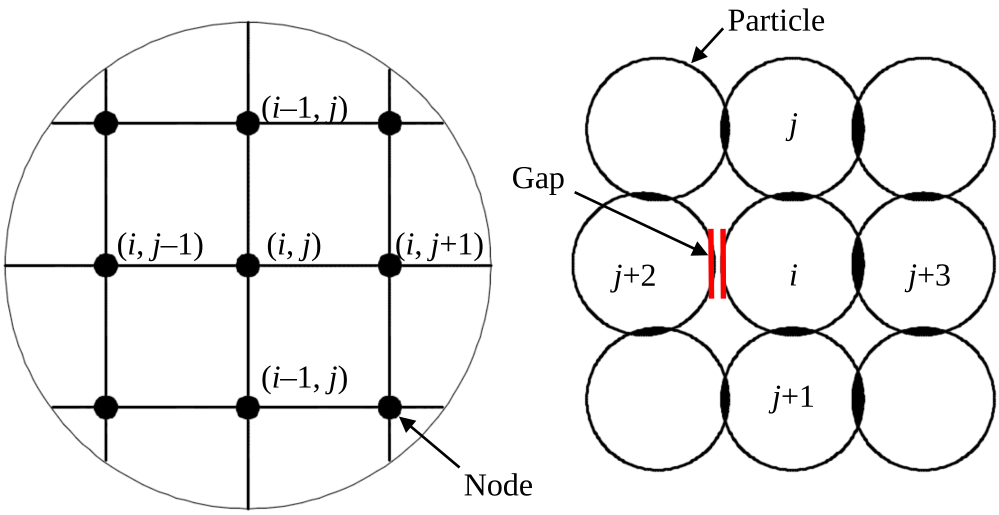

(a) (b)

Figure 7. Schematic illustrating EFG–DE domains: (a) EFG domain with difference nodes, and (b) DE domain with particles at contact.

Table 1 presents the sets of governing equations used in the EFG and DE domains respectively. These equations demonstrate the motions occurred in a time step increment from *t* to *t*+Δ*t*. The two sets of equations are tabularised to compare the difference in conception when computing nodes (or discs) motion. Specifically, in the continuum domain, an external force matrix is a major target; in the granular domain, internal disc–disc contact forces are computed to provide the force–displacement relationship. Regarding the equation solving processes, the continuum domain uses the Taylor expansion to obtain the recurrence relationship at the end of the time increment. The granular domain uses the central difference method and determines the velocity at $t+\frac{\Delta t}{2}$ which is known as the average speed during a time step increment. Extra rolling behavior at disc *i*, such as rolling angle θ_i, rolling velocity $\dot{\theta}_i$, and rolling acceleration $\ddot{\theta}_i$, was added in the DE analysis.

Table 1 Governing equations to depict the motion of elements in EFG and DE domains.

	EFG domain	DE domain
Displacement	$\boldsymbol{U}_{t+\Delta t} = \dfrac{\boldsymbol{F}_{t+\Delta t} + \boldsymbol{M}(\alpha_1 \boldsymbol{U}_t + \alpha_2 \dot{\boldsymbol{U}}_t + \alpha_3 \ddot{\boldsymbol{U}}_t)}{\alpha_1 \boldsymbol{M} + \bar{\boldsymbol{K}}}$ (49)	$(u_i)_{t+\Delta t} = (u_i)_t + (\dot{u}_i)_{t+\Delta t/2} \times \Delta t$ (50) $(\theta_i)_{t+\Delta t} = (\theta_i)_t + (\dot{\theta}_i)_{t+\Delta t/2} \times \Delta t$ (51)
Velocity	$\dot{\boldsymbol{U}}_{t+\Delta t} = \dot{\boldsymbol{U}}_t + (1-\beta_1)\Delta t \ddot{\boldsymbol{U}}_t + \beta_1 \Delta t \ddot{\boldsymbol{U}}_{t+\Delta t}$ (52)	$(\dot{u}_i)_{t+\Delta t/2} = (\dot{u}_i)_{t-\Delta t/2} + (\ddot{u}_i)_t \times \Delta t$ (53) $(\dot{\theta}_i)_{t+\Delta t/2} = (\dot{\theta}_i)_{t-\Delta t/2} + (\ddot{\theta}_i)_t \times \Delta t$ (54)
Acceleration	$\ddot{\boldsymbol{U}}_{t+\Delta t} = \alpha_1(\boldsymbol{U}_{t+\Delta t} - \boldsymbol{U}_t) - \alpha_2 \dot{\boldsymbol{U}}_t - \alpha_3 \ddot{\boldsymbol{U}}_t$ (55)	$(\ddot{u}_i)_t = (\sum_{j=1}^{N} F_{ij} / m_{p,i})\Delta t$ (56) $(\ddot{\theta}_i)_t = (\sum_{j=1}^{N} M_{ij} / I_i)\Delta t$ (57)
Force	External forces determined in terms of Eqs. (27–28)	$(F_{ij})_{t+\Delta t} = (F_{ij})_t + k(\dot{u}_i)_{t+\Delta t/2}\Delta t + \beta k(\dot{u}_i)_{t+\Delta t/2}\Delta t$ (58) $(M_{ij})_{t+\Delta t} = (M_{ij})_t + k_s\{(\dot{u}_i)_{t+\Delta t/2} s\} r_i \Delta t$ (59)

where in Eq (49), the parameters are respectively expressed as:

$$\bar{\boldsymbol{K}} = \boldsymbol{K} + \boldsymbol{K}^{\alpha} \tag{60}$$

$$\alpha_1 = \frac{2}{\beta_2 \Delta t^2} \tag{61}$$

$$\alpha_2 = \frac{2}{\beta_2 \Delta t} \tag{62}$$

$$\alpha_3 = \frac{1}{\beta_2} - 1 \tag{63}$$

where, two constants β_1 =1.5 and β_2 =1.6 are used as the Newmark parameters as per [26].

4. EXAMPLE PROBLEMS

Two example problems were examined and solved using the developed EFG–DE method, aiming to validate this coupling method. The first example problem is to assess a cantilever beam which is subjected to a disc acting at the end of the beam. The second example problem is developed based on the *Nine Disc Test* [36]. The test reproduces a bi-axial test on an assembly of nice discs. Contact force evolution and stress distribution between the discs are estimated. The two example problems consider multi-body interactions, but involve less number of nodes or discs than required in other large-scale problems. This means the computational costs are affordable, and these special settings satisfy the aim of developing and validating the EFG–DE method. The deformation, on both continuum and granular bodies, however, is executed in a large scale so that the advantages of the mesh free method can be demonstrated and confirmed.

4.1. Example 1

This section presents a study on the dynamic interaction that occurs between a disc and a cantilever beam. The EFG–DE method is applied to the example problem, and the numerical results are compared with the analytical solutions developed for the same example problem.

4.1.1. Problem description

In this example problem, the cantilever beam is fixed to a rigid surface, and the disc sits on the other end, as shown in Figure 8. The beam measures 1 (L) × 0.2 (H) × 0.025 (D) m. The material density of the beam is ρ_b = 2,000 kg/m³. The radius of the disc is r = 0.05 m, and its density is ρ_d = 1,000 kg/m³. It was assumed that the material of the beam exhibits linear elastic behavior with Young's modulus $E = 2.1\times10^8$ Pa and Poisson's ratio $\nu = 0.3$, and that the disc material is simulated with the linear contact model with stiffnesses of $k_n = k_s = 10^6$ N/m. The system is assumed un-damped (i.e., damping coefficient is zero).

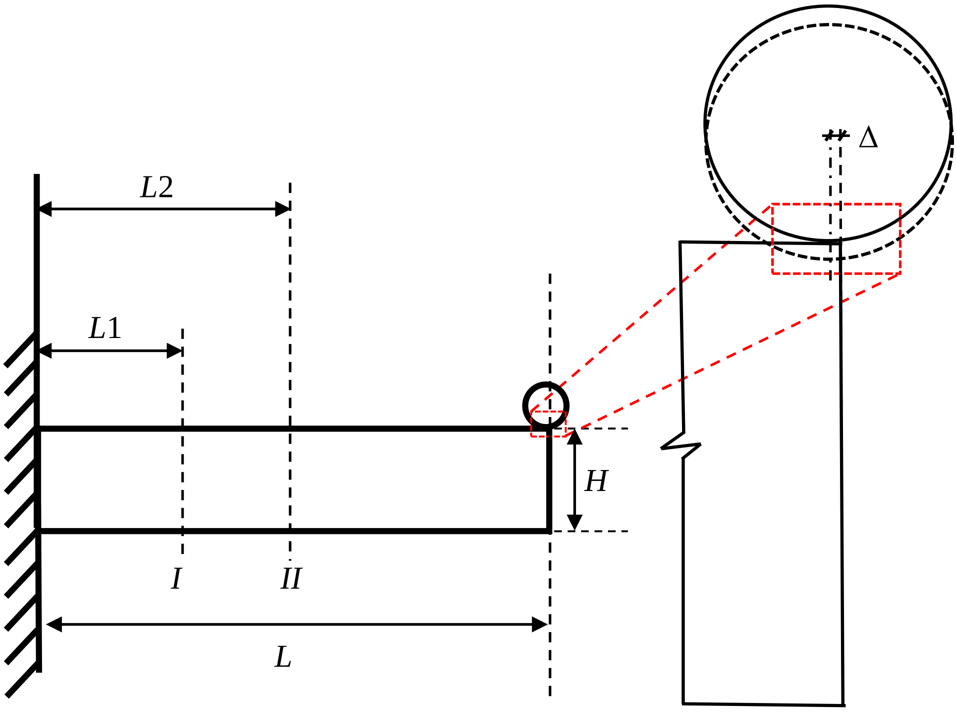

Figure 8. Schematic of the disc falling down against the end of the cantilever beam.

In the simulation, the beam is discretized into a node arrangement of 20×4. The node grid is refined by a 4×4 Gauss quadrature scheme. At time t = 0, the beam is at rest, and its upper–right boundary is in contact with the disc edge (no overlap or deformation). The disc centroid sits at a small distance $\Delta = 10^{-3}$ mm inward from the beam end, to ensure that the centroid falls inside the boundary of the beam. When t increases, the disc goes down under the gravity and penetrates the boundary of the beam. Meanwhile, the beam displaces, in particular at its end, forming a convex profile, prompting the disc to fall out.

4.1.2. Termination condition

The termination condition was determined in terms of the trajectory of the disc centroid.

The centroid tends to move outward when the beam is bent downward. Where the projection of the centroid falls out of the boundary of the beam, the interaction between the disc and beam becomes unstable and the simulation terminates. To determine the fall-off moment, the vertical displacements of the beam end and the disc centroid are captured and plotted with time as shown in Figure 9. Where the two displacement values disagree, the corresponding time is when the fall-off occurs. It is shown that the corresponding time point is t = 0.1431 s. It is noted that excellent agreement is obtained between the two displacement curves before this fall-off time point is reached, thus demonstrating the stability of the simulation.

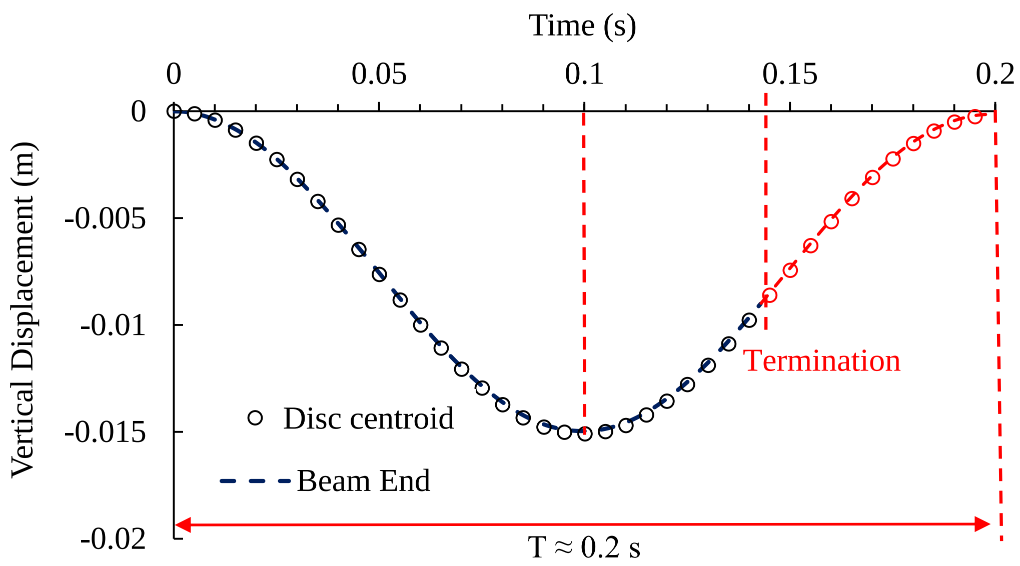

Figure 9. Displacement profile for the end of the beam and the centroid of the disc.

4.1.3. Model validation

The numerical results are compared with the analytical solutions developed for the same example problem. The problem was solved in a plane stress condition—a point load P acting at the upper right corner of the beam. According to Euler–Bernoulli beam theory, the axial stress, σ_{11}, and the deflection of the beam, w_x, are respectively expressed as:

$$\sigma_{11} = \frac{P(L-x)y}{I_m} \tag{64}$$

$$w(x) = \frac{Px^2(3L-x)}{6EI_m} \tag{65}$$

where (x, y) is the coordinate of the cross section of interest, and I_m is the moment of inertia of the beam.

The axial stress profiles at two cross sections I at L_1 = 0.3 m and II at L_2 = 0.5 m as shown in Figure 8 are obtained. For the simulation results, the axial stress at the same cross sections is captured. But, due to the beam acting without damping, the results where the beam is in its minimal acceleration $t = T/4$, are used. The results are presented in Figure 10. The axial stress is plot as a function of the vertical depth y for both the simulation and analytical results. At either of the cross sections, excellent agreement between the simulation and analytical results is obtained. Similarily sastisfactory agreement is obtained for the deflection profile of the beam, as presented in Figure 11. The results agreement verifies the capability of the EFG–DE model in simulating the dynamic response of the beam. Furthermore, the orthogonal basis function was used in the iterations, and this function avoids the occurrence of any ill-conditioned problems. The similar advantage in simulation stability is obtained due to the uses of the explicit–implicit algorithm for the time step and the penalty method for the boundary conditions.

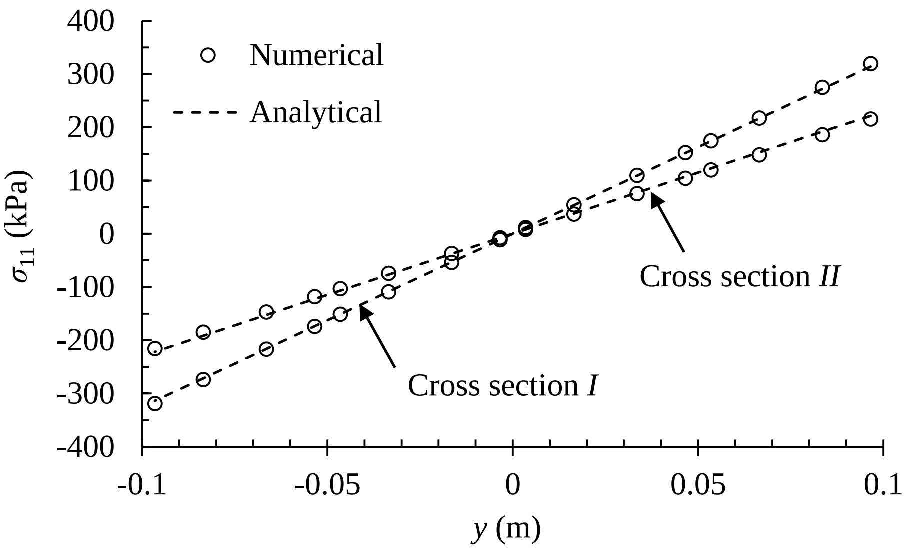

Figure 10. Axial stress profile plot at two cross sections of the cateliber beam.

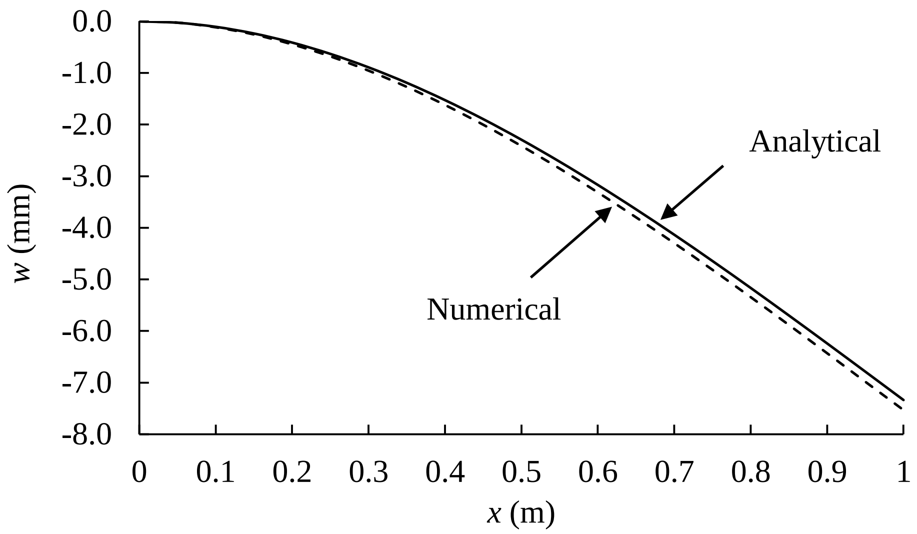

Figure 11. Deflection profile of the cantilever beam.

4.1.4. Variation of contact force with time

When the beam is subjected to a dynamic vibration, the contact forces acting on the boundary change over time. The results of the contact forces are provided in Figure 12.

In the figure, four critical time steps are identified: t = 0.001, 0.05, 0.1, and 0.143 s, which correspond to points (*a*), (*b*), (*c*), and (*d*) respectively. It is shown that the contact force gradually increases with time at the early stage of the test. At t = 0.05 s where the contact force equals the gravity force, the acceleration becomes zero, and then negative when the contact force exceeds the gravity. In the meantime, the disc velocity gradually decreases, but the contact force grows at a similar gradient. The contact force attains the peak value when t = 0.1 s, and at this moment, the disc attains the maximum displacement and penetration into the beam. After the peak point, the penetration releases gradually and the contact force goes down. At t = 0.143 s the contact force is less than the gravity, and the disc falls off the end of the beam.

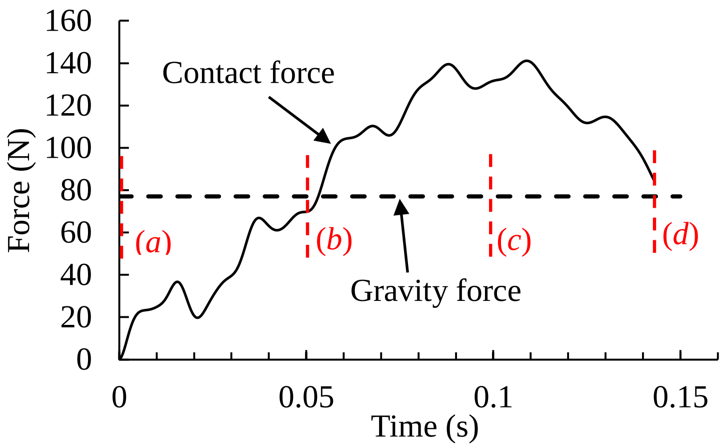

Figure 12. Development of disc–segment contact force over time.

4.2. Example 2

Example 2 was adapted from the *Nine Disc Test* [36]. In the original test, two pairs of plates were used to compress an assemblage of 9 discs. The plates were assumed ideally rigid. In example 2, the plates were allowed to deform to avoid the rigid body assumption. The *Nine Disc Test* is employed because of the following reasons: *a*) this test is designed to record the single contact force occurred between the discs and walls (or segments), enabling force gauging; *b*) the test can capture the effects of the plate deformation on the contact force; and, *c*) the test uses a small number of discs and facilitates contact detection and simulation in a short time period.

4.2.1. Problem description

An assembly of nine discs is sandwiched by two pairs of plates, as shown in Figure 13. The setup remains the same as in Cundall and Strack [36], except the left-hand side plate which is replaced with a deformable strip plate. This strip plate dimensions are 50 ($L1$) × 300 (H) × 1 (D) units, which enables a plane-stress scenario. As per Cundall and Strack [36], no physical unit but a number is provided to the properties of the setup or elements. Specifically, the radii are 50 units, the density is 1000 units, and the normal and shear stiffness are $k_n = k_s = 1.35\times10^9$ units for the linear contact model used for the discs. In the DE domain, the object wall is not assigned physical properties such as Young's modulus, Poisson's ratio or density. However, in the EFG domain (i.e., the strip plate), the material properties are specified in order to constitute a motion. These properties include Young's Modulus of 2.1×10^{14} units, Poisson's ratio of 0.3, the density of 2000 units. The plates were assumed to be undamped (c=0 in Eqs. (24)), and fixed at the top and bottom boundaries. To cross check the capacity of the proposed coupling method, we also simulated this example by using an FE-DE coupling method.

The EFG domain was replaced with the FE domain with a mesh coinciding with the background grid of EFG domain. The setting for DE domain remains the same as provided in Figure 13.

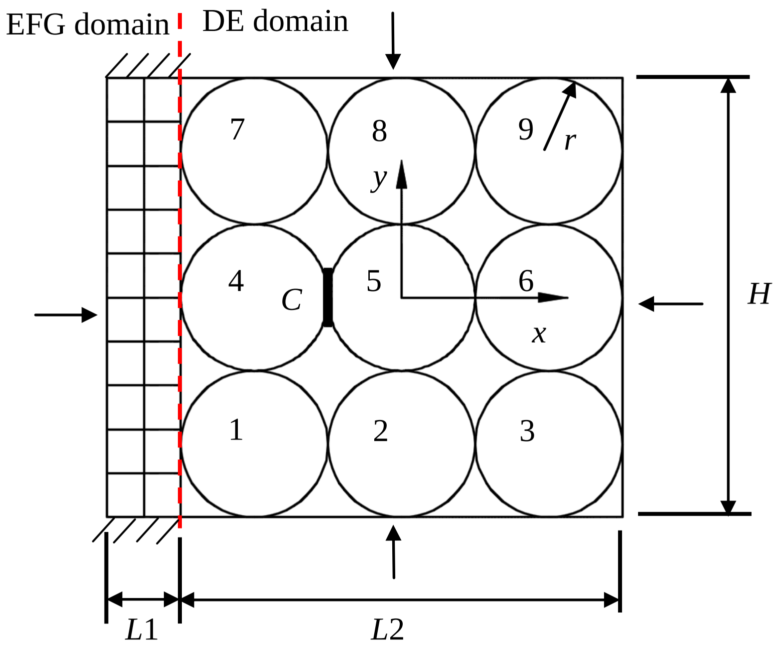

Figure 13. The nine disc test performed with deformable boundaries.

4.2.2. Model validation

In the simulation, the assembly of the nine discs is subjected to the bi-axial compression provided by the two pairs of plates. Two tests were performed. In Test 1, the plates travel at a velocity of 0.12 units and stop after 40 cycles. In Test 2, the velocity reduces to 0.04 units, but the plates continue to move until the 120th cycle. As per Cundall and Strack [36], both simulations continue to the 150th cycle and use a time step Δt = 0.01525 units and damping coefficient of 0.1. The continuum domain (i.e., the left-hand side plate) uses the cubic spine function [16] and a 3×11 nodal arrangement. In this arrangement, the assembly of discs falls into the choices of the disc–segment and disc–point contacts, depending on the disc locations as discussed in Figure 5.

The normal contact force at point *C* (i.e., the contact of discs 4 and 5) is examined. The results of the contact force are presented in Figure 14. The results include the simulations provided by the EFG–DE method, DEM, and Cundall and Strack [36]. In the DEM simulation, the plates were modeled as rigid walls and the test was reproduced using *PFC* programming. Excellent agreement is attained on both tests. In Test 1 however discrepancies occur in the early- to middle stage (i.e., before the 80th cycle). This means that the discs contact force is sensitive to the loading rate and the plate modulus. Specifically, when the rate is as low as in Test 2, the discrepancies fade off at the 20th cycle and are relatively small compared to the results arising from the rigid plate based simulations (i.e. the DEM and Cundall and Strack [36]). Where the rate is tripled as in Test 1, the discrepancies increase in amplitude and extension, meaning a stronger dynamic response. It is plausible to suggest that stronger dynamic responses of contact force occur where the loading rate is further increased or the plate modulus is decreased. Although the discrepancies exist, the trendline agreement on the two tests verifies the capability of the coupling method in approximating the dynamic response occurred between the continuum and granular domains.

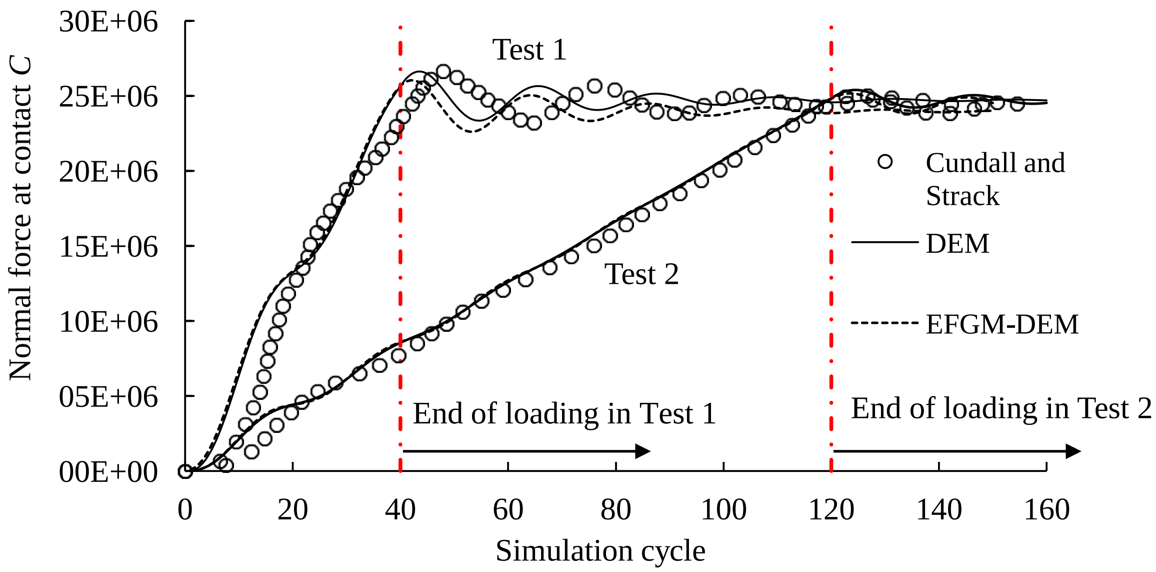

Figure 14. Normal force at contact *C* in standard unit versus simulation cycle determined by different simulation methods.

FE-DE simulations provide some new outcomes. It appears that Newmark β method was only conditionally stable in the FE domain, probably due to the relatively large mesh sizes used. The allowable maximum time step Δt was coupling method dependent. For example, given the modulus, the time step for a stable simulation is Δt = 0.01525 for EFG–DE coupling and is reduced to Δt = 0.00001525 for FE–DE coupling. It appears that EFG–DE program was stable under a lager time step. Even so, the FE method offers advantage in simulation efficiency in simulating small displacement problems, partially due to it updating interfacial contact forces be means of movable loads [47]. This offers simplicity as opposed to the interaction adopted in the EFG–DE coupling. On large-scale displacement problems, FE simulation cost can escalate due to re-meshing requirements as per Liu and Gu (2005).

4.2.3. Influence of Young's modulus

To gain an insight into the effects of plate deformation on the discs contact force, additional EFG–DE simulations were performed on scenarios where Young's modulus for the left-hand side plate was varied. Where the modulus is small, a large contact overlap tends to occur, and the results likely become unstable which is called *contact buckling* [37]. In this circumstance, as pointed out by Kanto and Yagawa [48], numerical oscillation may occur at contact because of the discontinuous velocity and acceleration when enforcing geometric compatibility. To prevent a severe contact overlap, Young's modulus was trialed and assigned $E = 2.1\times10^{14}$, 2.1×10^{13}, 2.1×10^{12}, and 1×10^{10} units respectively for the plate. Similarly, Tests 1 and 2 that were used in the *nine disc test* were performed to examine the effects of the simulation cycles on the results. The results of the normal force at contact *C* obtained in the two tests under the varying plate modulus conditions are presented in Figure 15. In either test, the plate modulus noticeably influences the development of the contact force. The higher the modulus is, the greater the contact force will be. This relationship is more pronounced in stage two of the tests, i.e., the period when the plates stop mvoing and compressing the assembly of discs. Where the plate stiffness is relatively high, i.e., $E \geq 2.1\times10^{13}$ units, the result curves coincide and approach equilibrium at the end of simulations. This trendline agrees with the results obtained in the DEM simulation (Figure 14). This means that the plate modulus of $E \geq 2.1\times10^{13}$ units is high enough to satisfy the rigid assumption made in the DEM simulation. Where the plate is less stiff, the contact force attenuates over time. This is probably caused by the discs penetrate the plate when the plate deforms, decreasing the overlap at contact *C*.

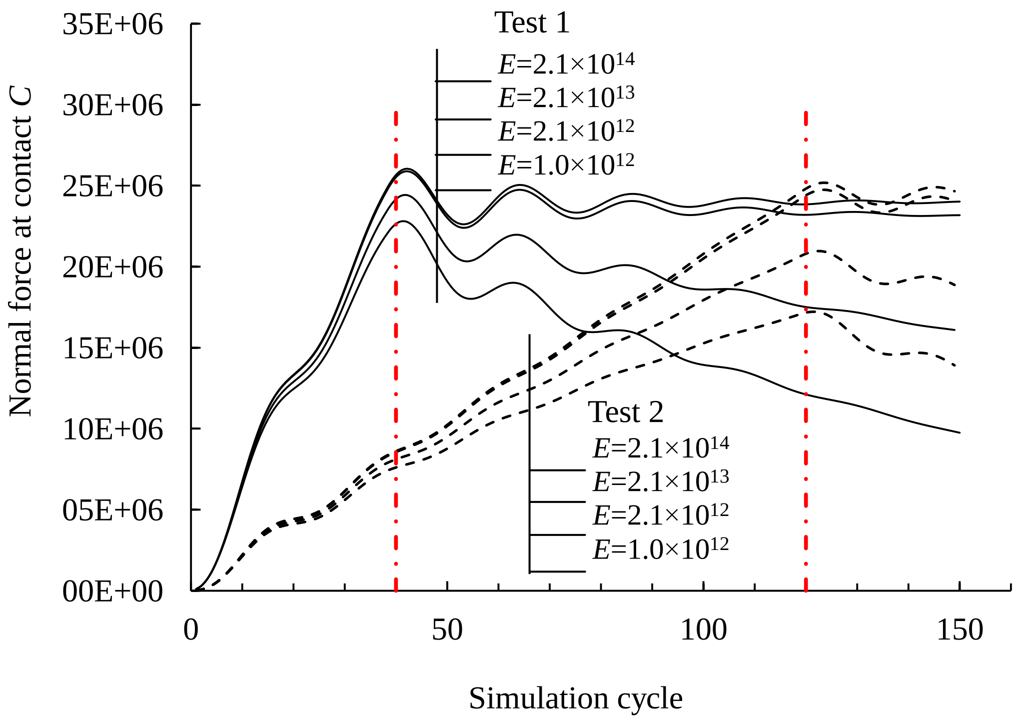

Figure 15. The relationship between the contact force in standard unit and the cycles for test scenarios that assign the plates with varying Young's moduli in standard unit.

To gain a further insight into the response of a less stiff plate (i.e., E = 1.0×10^{12} units), the deformation occurred to the boundary nodes of the plate as shown in Figure 16 is examined. An enlarged view of the nodes displacement captured at the 40th cycle is shown in Figure 17. Due to the use of the deformable plate, the actual displacement at the plate boundary is not uniform. The central nodes displace significantly greater than those occurred on the upper and bottom plates. The location dependency agrees with the observations occurred in the tri-axial tests [42, 49] where the central section of the samples dilated and thus presented greater deformation.

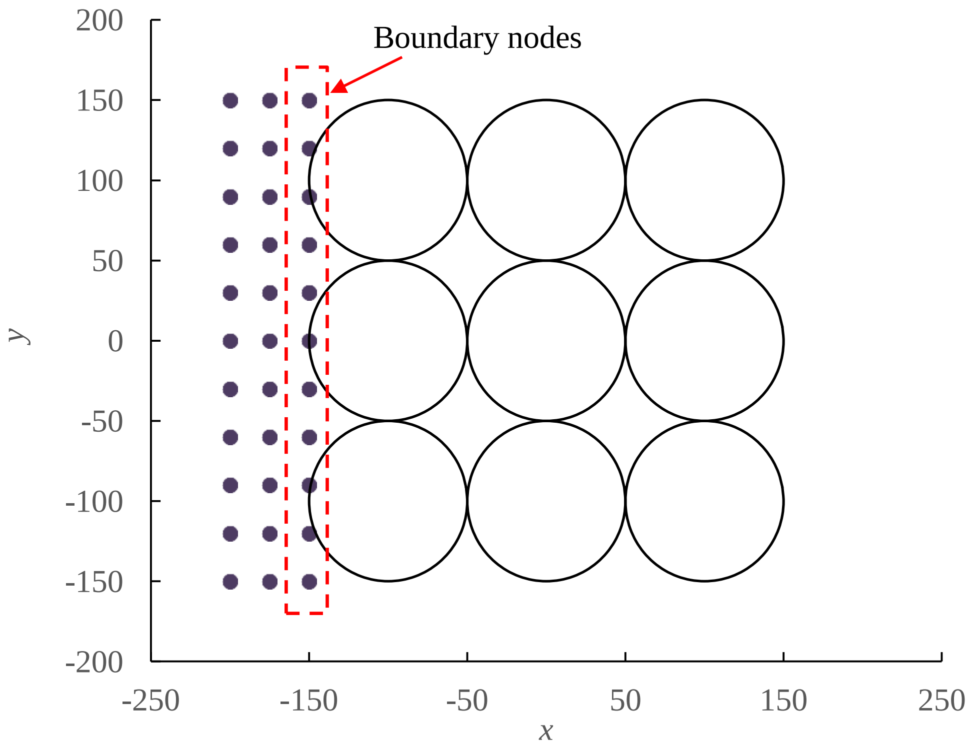

Figure 16. Boundary nodes location on the plate–discs interface examined for the plate deformation.

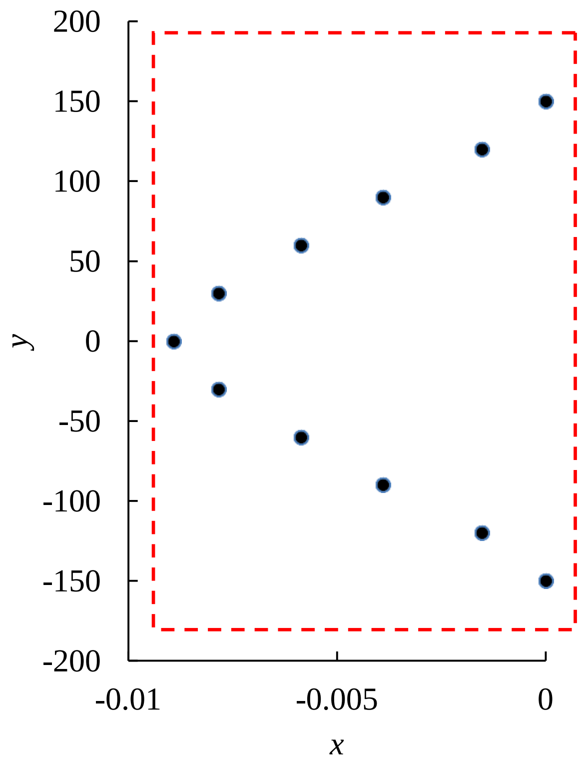

Figure 17. Displacement in standard unit of the boundary nodes on the plate–discs interface recorded at the 40th cycle.

5. CONCLUSIONS

This paper presents an element-free, multiscale EFG–DE coupling method. This method is developed to simulate multibody interactions, in particular, the continuum–granular contact problems. This method uses a transient disc–segment contact algorithm for the contact problems and is applied to two example problems. This study arrives at the following conclusions.

The coupled EFG–DE method is free of meshing or re-meshing, thus enabling reasonable computation costs and stable calculation. This method applies the

Newmark-β method to the continuum and the central difference method to the granular domain to solve the dynamic problem in a discrete form. This method uses an explicit–implicit time scheme and attains satisfactory computation stability. This method develops a transient contact detection algorithm which enables accurate, seamless force exchange on the domains interface, and accounts for deformable boundaries. The method is applied to two example problems and verified against the existing analytical and simulation results, thus confirming its capabilities in simulating dynamic interaction occurred between continuum and granular media. As opposed to other coupled numerical approaches (e.g., FEM−DEM or FEM−EFGM), this current method is capable to conduct numerical analysis with less external interventions. In addition the method is able to separate different domains and examine the particular behaviour of interest. It is envisaged that the proposed method will be applied to large-scale, multi-body interaction problems to further verify its performance.

ACKNOWLEDGEMENTS

This research was funded by the Australian Government through the Australian Research Council (project No. DP140103004). Professional editor, Leticia Mooney, provided copyediting and proofreading services, according to the guidelines laid out in the university-endorsed national ‘Guidelines for editing research theses’.

REFERENCES

[1] Elmekati A, Shamy UE. A practical co-simulation approach for multiscale analysis of geotechnical systems. Comput Geotech 2010;37(4):494-503.

[2] Azevedo NM, Lemos JV. Hybrid discrete element/finite element method for fracture analysis. Computer Methods in Applied Mechanics and Engineering 2006;195(33-36):4579-93.

[3] Tran QA, Villard P, Dias D. Discrete and continuum numerical modeling of soil arching between piles. International Journal of Geomechanics 2019;19(2).

[4] Munjiza AA. The Combined Finite-Discrete Element Method. West Susses, England: John Wiley & Sons, 2004.

[5] Onate E, Rojek J. Combination of discrete element and finite element methods for dynamic analysis of geomechanics problems. Computer Methods in Applied Mechanics and Engineering 2004;193(27):3087-128.

[6] Li M, Yu H, Wang J, Xia X, Chen J. A multiscale coupling approach between discrete element method and finite difference method for dynamic analysis. International Journal for Numerical Methods in Engineering 2015;102(1):1-21.

[7] Guo N, Zhao J. 3D multiscale modeling of strain localization in granular media. Comput Geotech 2016;80(360-72.

[8] Fakhimi A. A hybrid discrete-finite element model for numerical simulation of geomaterials. Comput Geotech 2009;36(3):386-95.

[9] An HM, Liu HY, Han H, Zheng X, Wang XG. Hybrid finite-discrete element

modelling of dynamic fracture and resultant fragment casting and muck-piling by rock blast. Comput Geotech 2017;81(322-45.

[10] Chen H, Zhang Y, Zang M, Hazell PJ. An accurate and robust contact detection algorithm for particle‐solid interaction in combined finite‐discrete element analysis. International Journal for Numerical Methods in Engineering 2015;103(8):598-624.

[11] Zang M, Gao W, Lei Z. A contact algorithm for 3D discrete and finite element contact problems based on penalty function method. Computational Mechanics 2011;48(5):541-50.

[12] Zheng Z, Zang M, Chen S, Zhao C. An improved 3D DEM-FEM contact detection algorithm for the interaction simulations between particles and structures. Powder Technology 2017;305(308-22.

[13] Ghazavi Baghini E, Toufigh MM, Toufigh V. Analysis of pile foundations using natural element method with disturbed state concept. Comput Geotech 2018;96(178-88.

[14] Zhao X, Xu J, Zhang Y, Xiao Z. Coupled DEM and FDM algorithm for geotechnical analysis. International Journal of Geomechanics 2018;18(6).

[15] Chua KH, Fwa TF, Shein A. A finite difference model for computing thermal conductivity of granular materials. Comput Geotech 1992;14(1):43-55.

[16] Liu G-R, Gu Y-T. An Introduction to Meshfree Methods and Their Programming. The Netherlands: Springer, 2005.

[17] Ghazavi Baghini E, Toufigh MM, Toufigh V. Mesh-free analysis applied in reinforced soil slopes. Comput Geotech 2016;80(322-32.

[18] Hassanzadeh M, Tohidvand HR, Hajialilue-Bonab M, Javadi AA. Scaled boundary point interpolation method for seismic soil-tunnel interaction analysis. Comput Geotech 2018;101(208-16.

[19] Belytschko T, Lu YY, Gu L. Element‐free Galerkin methods. International Journal for Numerical Methods in Engineering 1994;37(2):229-56.

[20] Krysl P, Belytschko T. Analysis of thin shells by the element-free Galerkin method. International Journal of Solids and Structures 1996;33(20-22):3057-80.

[21] Belytschko T, Gu L, Lu Y. Fracture and crack growth by element free Galerkin methods. Model Simul Mater Sc 1994;2(3A):519.

[22] Lu Y, Belytschko T, Tabbara M. Element-free Galerkin method for wave propagation and dynamic fracture. Computer Methods in Applied Mechanics and Engineering 1995;126(1-2):131-53.

[23] Singh I. Application of meshless EFG method in fluid flow problems. Sadhana 2004;29(3):285-96.

[24] Samimi S, Pak A. Three-dimensional simulation of fully coupled hydro-mechanical behavior of saturated porous media using Element Free Galerkin (EFG) method. Comput Geotech 2012;46(75-83.

[25] Rao BN. Coupled meshfree and fractal finite element method for unbounded problems. Comput Geotech 2011;38(5):697-708.

[26] Zhang Z, Hao S, Liew K, Cheng Y. The improved element-free Galerkin method for two-dimensional elastodynamics problems. Engineering Analysis with Boundary

Elements 2013;37(12):1576-84.

[27] Chehel Amirani M, Nemati N. Simulation of two dimensional unilateral contact using a coupled FE/EFG method. Engineering Analysis with Boundary Elements 2011;35(1):96-104.

[28] Rajesh KN, Rao BN. Coupled meshfree and fractal finite element method for mixed mode two-dimensional crack problems. International Journal for Numerical Methods in Engineering 2010;84(5):572-609.

[29] Shedbale AS, Singh IV, Mishra BK. A coupled FE–EFG approach for modelling crack growth in ductile materials. Fatigue and Fracture of Engineering Materials and Structures 2016;39(10):1204-25.

[30] Ullah Z, Coombs WM, Augarde CE. An adaptive finite element/meshless coupled method based on local maximum entropy shape functions for linear and nonlinear problems. Computer Methods in Applied Mechanics and Engineering 2013;267(111-32.

[31] Guo X, Yang H. Solving viscoelastic problems with cyclic symmetry via a temporally adaptive EFG-SB partitioning algorithm. Engineering with Computers 2019;35(1):101-13.

[32] Zhang Z, Liew KM, Cheng Y. Coupling of the improved element-free Galerkin and boundary element methods for two-dimensional elasticity problems. Engineering Analysis with Boundary Elements 2008;32(2):100-7.

[33] Gu YT, Liu GR. A coupled element free Galerkin/boundary element method for

stress analysis of tow-dimensional solids. Computer Methods in Applied Mechanics and Engineering 2001;190(34):4405-19.

[34] Chen J-S, Wang D. Extended meshfree method for elastic and inelastic media. In: Griebel M, Schweitzer MA, editors. Meshfree Methods for Partial Differential Equations II: Springer-Verlag Berlin Heidelberg, 2005. p. 39-54.

[35] Lu YY, Belytschko T, Gu L. A new implementation of the element free Galerkin method. Computer Methods in Applied Mechanics and Engineering 1994;113(3-4):397-414.

[36] Cundall PA, Strack OD. A discrete numerical model for granular assemblies. Geotechnique 1979;29(1):47-65.

[37] Nakashima H, Oida A. Algorithm and implementation of soil–tire contact analysis code based on dynamic FE–DE method. Journal of Terramechanics 2004;41(2):127-37.

[38] Gross L, Bourgouin L, Hale AJ, Mühlhaus HB. Interface modeling in incompressible media using level sets in Escript. Physics of the Earth and Planetary Interiors 2007;163(1-4):23-34.

[39] Xiao SP, Belytschko T. A bridging domain method for coupling continua with molecular dynamics. Computer Methods in Applied Mechanics and Engineering 2004;193(17-20):1645-69.

[40] Lei Z, Zang M. An approach to combining 3D discrete and finite element methods based on penalty function method. Computational Mechanics 2010;46(4):609-19.

[41] Muth B, Müller M-K, Eberhard P, Luding S. Collision detection and administration

methods for many particles with different sizes. In: Cleary P, editor. Discrete Element Methods, DEM 07 Brisbane, Australia: Minerals Engineering Int., 2007. p. 1-18.

[42] Fakhimi A. A hybrid discrete–finite element model for numerical simulation of geomaterials. Comput Geotech 2009;36(3):386-95.

[43] Zuohui P. Treatment of point loads in element free Galerkin method (EFGM). International Journal for Numerical Methods in Biomedical Engineering 2000;16(5):335-41.

[44] Belytschko T, Liu WK, Moran B, Elkhodary K. Nonlinear Finite Elements for Continua and Structures. 2nd ed. West Susses, United Kingdom: John Wiley & Sons, 2013.

[45] O'Sullivan C, Bray JD. Selecting a suitable time step for discrete element simulations that use the central difference time integration scheme. Engineering Computations 2004;21(2/3/4):278-303.

[46] Elmekati A, El Shamy U. A practical co-simulation approach for multiscale analysis of geotechnical systems. Comput Geotech 2010;37(4):494-503.

[47] Rieker JR, Lin YH, Trethewey MW. Discretization considerations in moving load finite element beam models. Finite Elem Anal Des 1996;21(3):129-44.

[48] Kanto Y, Yagawa G. A dynamic contact buckling analysis by the penalty finite element method. International Journal for Numerical Methods in Engineering 1990;29(4):755-74.

[49] Oda M. Deformation mechanism of sand in triaxial compression tests. Soils and

Foundations 1972;12(4):45-63.